Six-qubit two-photon hyperentangled cluster states: Characterization and application to quantum computation

Giuseppe Vallone,[1,2,*] Gaia Donati,[2,*] Raino Ceccarelli,[2,*] and Paolo Mataloni[2,3,*]
[1]*Museo Storico della Fisica e Centro Studi e Ricerche Enrico Fermi, Via Panisperna 89/A, Compendio del Viminale, Roma I-00184, Italy*
[2]*Dipartimento di Fisica, Università Sapienza di Roma, Roma I-00185, Italy*
[3]*Istituto Nazionale di Ottica (INO-CNR), L.go E. Fermi 6, I-50125 Florence, Italy*
(Received 11 November 2009; published 4 May 2010)

Six-qubit cluster states built on the simultaneous entanglement of two photons in three independent degrees of freedom, that is, polarization and a double longitudinal momentum, have been recently demonstrated. We present here the peculiar entanglement properties of the linear cluster state $|\widetilde{\mathrm{LC}}_6\rangle$ related to the three degrees of freedom. This state has been adopted to realize various kinds of controlled NOT (CNOT) gates, obtaining high values of the fidelity of the expected output states for all considered cases. Our results demonstrate that these states may represent a promising approach toward scalable quantum computation in a medium-term time scale. The future perspectives of a *hybrid* approach to one-way quantum computing based on multiple degrees of freedom and multiphoton cluster states are also discussed in the conclusion of this article.

DOI: 10.1103/PhysRevA.81.052301 PACS number(s): 03.67.Bg, 42.65.Lm

I. INTRODUCTION

Multiqubit graph states [1] are a basic resource for a number of important quantum-information applications. These states have been proposed in particular for advanced tests of quantum nonlocality in which the violation of local realism increases exponentially with the number of qubits [2–5] and for the realization of quantum-computation algorithms of increasing complexity in the one-way model [6,7]. Other application fields deal with quantum communication [8] and quantum error correction [9].

In recent years, photon cluster states of four, six, and up to ten qubits have been realized by different approaches and used to deeply investigate the peculiar properties of high-dimensional entanglement [10] and to perform basic quantum computation algorithms [11,12].

Two strategies are generally used to create multiqubit cluster states: one consists of increasing the number of entangled photons [13–17]; the second one is based on the encoding of more qubits in different degrees of freedom of the particles [11,12,18,19]. By the first approach, some examples of four- and six-photon [13–16] cluster states have been experimentally demonstrated, up to now, with very low rates. The second approach, which is based on two-photon hyperentanglement, has been used to create two-photon, four-qubit cluster states [18–28]. By using hyperentanglement, five photons have been recently entangled in ten qubits encoded in the polarization and longitudinal momentum degrees of freedom (DOFs) [19].

The advantages of the hyperentangled-state approach, as far as generation rate, detection efficiency rate and fidelity of the states are concerned, have been already demonstrated [11,12]. These properties have been very recently confirmed by the realization of the linear two-photon, six-qubit cluster state $|\widetilde{\mathrm{LC}}_6\rangle$, starting from the triple entanglement of two photons in three independent DOFs [29], namely, the polarization and a double longitudinal momentum. The $|\widetilde{\mathrm{LC}}_6\rangle$ is the only distribution of six qubits between two particles whose perfect correlations have the same nonlocality as those of the six-qubit Greenberger-Horne-Zeilinger state [5], but only requires two separated carriers [4].

In this article we give a detailed characterization of the $|\widetilde{\mathrm{LC}}_6\rangle$ state realized by using the triple hyperentanglement of two photons and demonstrate its feasibility for one-way quantum computation by the realization of different kinds of controlled-NOT (CNOT) gates.

The article is organized as follows. In Sec. II we describe the realization of the six-qubit linear cluster state, derived from the application of suitable controlled-PHASE (CPHASE) gates to a six-qubit hyperentangled state. Section III reports on the characterization of the $|\widetilde{\mathrm{LC}}_6\rangle$ state by a sequence of quantum tomographic reconstructions performed in the three DOFs. Section IV describes how the CNOT gate has been efficiently realized with six qubits. Finally, the future perspectives of the realization of multiqubit cluster states built on an increasing number of photon DOFs are discussed in the conclusions of Sec. V.

II. GENERATION OF THE SIX-QUBIT CLUSTER STATE

Cluster states are peculiar entangled states associated to n-dimensional lattices where each vertex i represents a qubit and connections between vertices correspond to Ising interactions between the two-level quantum systems. Two-dimensional lattices have proved to be a universal resource for quantum computation (QC) [6]; from here on, we shall then restrict ourselves to the case $n = 2$. The explicit expression of a cluster state is obtained by preparation of each qubit in the state $|+\rangle_i = \frac{1}{\sqrt{2}}(|0\rangle_i + |1\rangle_i)$ and subsequent application of a CPHASE gate, CZ_{ij}, between two adjacent vertices i and j. We have

$$\mathrm{CZ}_{ij} = |0\rangle_i\langle 0| \otimes \mathbb{1}_j + |1\rangle_i\langle 1| \otimes Z_j, \tag{1}$$

where $\mathbb{1}$ is the identity operator. From now we will use the following simplified notation for the Pauli operators $\sigma_z^{(i)} \equiv Z_i$ and analogous relations for $\sigma_x^{(i)}$ and $\sigma_y^{(i)}$.

*http://quantumoptics.phys.uniroma1.it/

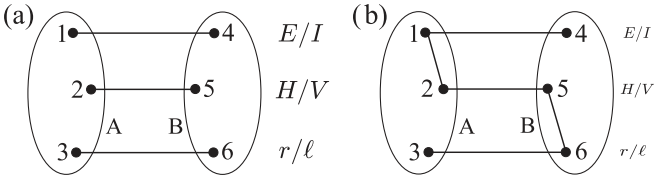

FIG. 1. (a) Graph associated to the hyperentangled state $|\mathrm{HE}_6\rangle$. Each set represents a photon and every vertex is associated to a qubit. Qubits 1 and 4 are encoded in the E/I DOF, qubits 2 and 5 in polarization, and qubits 3 and 6 in the r/ℓ DOF. See text for further details. (b) Graph associated to the two-photon six-qubit linear cluster state $|\mathrm{LC}_6\rangle$. $|\mathrm{LC}_6\rangle$ can be obtained from $|\mathrm{HE}_6\rangle$ by applying two CZ operations between qubits belonging to different DOFs.

For a lattice $\mathcal{L}$ with N sites, the corresponding cluster state can then be written as

$$|\Phi_N^{\mathcal{L}}\rangle = \left(\prod_{i,j \text{ linked}} \mathrm{CZ}_{ij}\right)|+\rangle^N, \tag{2}$$

where $|+\rangle^N = |+\rangle_1 \otimes |+\rangle_2 \otimes \cdots \otimes |+\rangle_N$.

In general, the cluster state associated to a specific graph can be equivalently defined as the only state satisfying the eigenvalue equations

$$g_i|\Phi_N^{\mathcal{L}}\rangle = |\Phi_N^{\mathcal{L}}\rangle \tag{3}$$

for every lattice vertex i, where the operators

$$g_i = X_i \bigotimes_{j\in\mathcal{N}_i} Z_j \tag{4}$$

are known as the stabilizer generators for the cluster state. $\mathcal{N}_i$ is the set of vertices connected with the vertex i.

The linear cluster state $|\mathrm{LC}_6\rangle$ is the state associated to the lattice shown in Fig. 1(b). We generated a six-qubit, two-photon linear cluster state $|\widetilde{\mathrm{LC}}_6\rangle$, equivalent to $|\mathrm{LC}_6\rangle$ up to single qubit unitary transformations, starting from the hyperentangled state $|\widetilde{\mathrm{HE}}_6\rangle$ and exploiting the three DOFs of polarization and two different kinds of longitudinal momentum. To show that the cluster state $|\widetilde{\mathrm{LC}}_6\rangle$ obtained in the laboratory is equivalent to $|\mathrm{LC}_6\rangle$, we start describing the source of the hyperentangled state $|\widetilde{\mathrm{HE}}_6\rangle$, the first step for the generation of the linear cluster $|\widetilde{\mathrm{LC}}_6\rangle$.

The two-photon, six-qubit source, extensively described elsewhere [22,23,29], consists of a continuous-wave (cw), vertically polarized Ar^+ laser beam ($P = 50$ mW, $\lambda_p = 364$ nm) interacting through spontaneous parametric down-conversion (SPDC) with a Type I, 0.5-mm-thick β barium borate (BBO) crystal. The nonlinear interaction between the laser beam and the BBO crystal produces degenerate photon pairs at wavelength $\lambda = 728$ nm, entangled in polarization and belonging to the surfaces of an emission cone. Referring to Fig. 2(a), the insertion of a holed mask allows us to select four pairs of correlated spatial modes from the conical surface, which is all we need for the creation of the hyperentangled state $|\widetilde{\mathrm{HE}}_6\rangle$. The labels used to identify the selected modes require some explanation [cf. Fig. 2(b)]: The distinction between left and right modes provides us with the first longitudinal momentum DOF (r/ℓ, also known as the linear momentum $\mathbf{k}$), while distinguishing between external and internal modes supplies the second momentum DOF (E/I). Moreover, the conical emission of the BBO crystal can be divided into an "up" circular half and a "down" one with respect to an ideal horizontal line passing through the center of the mask. Every mode belonging to the "up" half shall be associated to carrier photon A; an analogous correspondence is adopted for the "down" half and the second carrier photon B. By doing so we have at our disposal two SPDC photons, A and B, to each of which we associate three different qubits corresponding to the three DOFs (polarization and first and second momentum) introduced earlier in this article.

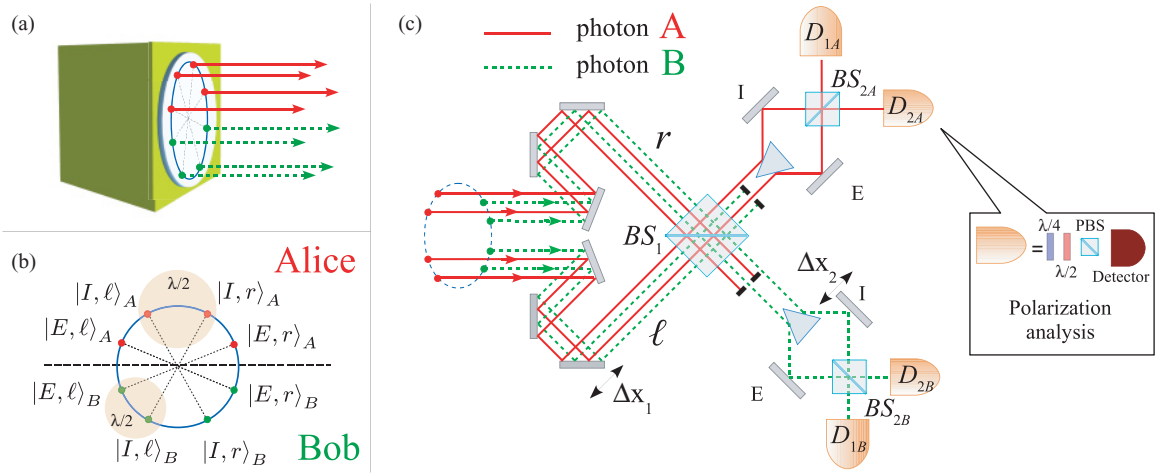

FIG. 2. (Color online) Setup of the experiment. (a) Source (green box) of the eight-mode hyperentangled state. A detailed description of the source is given in [22,23,29]. (b) Mode labeling. Upper (lower) modes correspond to Alice (Bob) photon. For each photon we indicate with $|r\rangle$ ($|\ell\rangle$) the right (left) modes and with $|I\rangle$ ($|E\rangle$) the internal (external) modes. We also show the two half-wave plates ($\lambda/2$) used to transform the hyperentangled state $|\widetilde{\mathrm{HE}}_6\rangle$ to the cluster state $|\widetilde{\mathrm{LC}}_6\rangle$. The $\lambda/2$ on the I modes of photon A is oriented at 45° while the $\lambda/2$ on the ℓ modes of photon B is oriented at 0°. (c) Measurement scheme. The momentum measurement setup consists of two chained interferometers, the first (BS_1) measuring the r/ℓ qubit, while the second (BS_{2A} and BS_{2B}) measuring the I/E qubit. Polarization analysis is performed by standard wave plates and polarizing beam splitters (PBS). Path delays Δx_1 and Δx_2 are varied to obtain the optimal temporal superposition of the modes, respectively, in the first and second interferometers.

By appropriately setting the phase of each pair of modes, the source generates the hyperentangled state $|\widetilde{\mathrm{HE}}_6\rangle$, explicitly written as

$$\begin{aligned}|\widetilde{\mathrm{HE}}_6\rangle &= \frac{1}{\sqrt{2}}(|HH\rangle_{AB} - |VV\rangle_{AB}) \otimes \frac{1}{2}(|Er\rangle_A|E\ell\rangle_B \\ &\quad + |E\ell\rangle_A|Er\rangle_B + |Ir\rangle_A|I\ell\rangle_B + |I\ell\rangle_A|Ir\rangle_B) \\ &= \frac{1}{\sqrt{2}}(|EE\rangle_{AB} + |II\rangle_{AB}) \otimes \frac{1}{\sqrt{2}}(|HH\rangle_{AB} \\ &\quad - |VV\rangle_{AB}) \otimes \frac{1}{\sqrt{2}}(|r\ell\rangle_{AB} + |\ell r\rangle_{AB}). \qquad (5)\end{aligned}$$

It comes out that the state $|\widetilde{\mathrm{HE}}_6\rangle$ is given by a tensor product of three maximally entangled states, one for each DOF.

By setting the following correspondences between physical and computational qubits,

$$\{|E\rangle_A, |I\rangle_A\} \to \{|0\rangle_1, |1\rangle_1\}, \qquad (6a)$$
$$\{|H\rangle_A, |V\rangle_A\} \to \{|0\rangle_2, |1\rangle_2\}, \qquad (6b)$$
$$\{|r\rangle_A, |\ell\rangle_A\} \to \{|0\rangle_3, |1\rangle_3\}, \qquad (6c)$$
$$\{|E\rangle_B, |I\rangle_B\} \to \{|0\rangle_4, |1\rangle_4\}, \qquad (6d)$$
$$\{|H\rangle_B, |V\rangle_B\} \to \{|0\rangle_5, |1\rangle_5\}, \qquad (6e)$$
$$\{|r\rangle_B, |\ell\rangle_B\} \to \{|0\rangle_6, |1\rangle_6\}, \qquad (6f)$$

we can express the state (5) as

$$|\widetilde{\mathrm{HE}}_6\rangle = \mathsf{H}_2 X_3 \mathsf{H}_3 \mathsf{H}_4 Z_5 |\mathrm{HE}_6\rangle, \qquad (7)$$

where $|\mathrm{HE}_6\rangle$ is the state associated to the graph shown in Fig. 1(a) and H_i is the Hadamard operator acting on qubit i. From the definition of graph states in Eq. (2), $|\mathrm{LC}_6\rangle$ is obtained from the graph state $|\mathrm{HE}_6\rangle$ by the application of the two-qubit gates CZ_{12} and CZ_{56}.

We build the state $|\widetilde{\mathrm{LC}}_6\rangle$ by applying the gates CX_{12} and CZ_{56} to the hyperentangled state $|\widetilde{\mathrm{HE}}_6\rangle$. The gate CX is defined as $\mathrm{CX}_{ij} = |0\rangle_i\langle 0| \otimes \mathbb{1}_j + |1\rangle_i\langle 1| \otimes X_j$. We are now in the position to state the relation between the state $|\widetilde{\mathrm{LC}}_6\rangle$ and the state $|\mathrm{LC}_6\rangle$:

$$\begin{aligned}|\widetilde{\mathrm{LC}}_6\rangle &= \mathrm{CX}_{12}\mathrm{CZ}_{65}|\widetilde{\mathrm{HE}}_6\rangle \\ &= \mathrm{CX}_{12}\mathrm{CZ}_{65}(\mathsf{H}_2 X_3 \mathsf{H}_3 \mathsf{H}_4 Z_5)|\mathrm{HE}_6\rangle \\ &= (\mathsf{H}_2 X_3 \mathsf{H}_3 \mathsf{H}_4 Z_5)\mathrm{CZ}_{12}\mathrm{CZ}_{65}|\mathrm{HE}_6\rangle \\ &= \mathsf{H}_2 X_3 \mathsf{H}_3 \mathsf{H}_4 Z_5 |\mathrm{LC}_6\rangle. \qquad (8)\end{aligned}$$

The previous relations can be easily demonstrated by using the property $\mathrm{CX}_{ij}\mathsf{H}_j = \mathsf{H}_j\mathrm{CZ}_{ij}$. We thus see that the generated cluster state $|\widetilde{\mathrm{LC}}_6\rangle$ is equivalent to the linear six-qubit, two-photon cluster state $|\mathrm{LC}_6\rangle$ up to the unitary transformation $[\mathsf{H}_2 X_3 \mathsf{H}_3 \mathsf{H}_4 Z_5]$ consisting of single-qubit unitaries. In the generated state, qubits 1 and 4 are encoded in the E/I longitudinal momentum DOF, qubits 2 and 5 in the polarization variable, and qubits 3 and 6 in the r/ℓ momentum DOF (see Fig. 1). Specifically, the relation given in (8) between $|\widetilde{\mathrm{LC}}_6\rangle$ and $|\mathrm{LC}_6\rangle$ implies that $|\widetilde{\mathrm{LC}}_6\rangle$ is the only common eigenstate of the generators $\{\widetilde{g}_i\}$ obtained from $\{g_i\}$ by changing $X_2 \leftrightarrow Z_2$, $X_3 \to -Z_3$, $Z_3 \to X_3$, $X_4 \leftrightarrow Z_4$, and $X_5 \to -X_5$.

Starting from Eq. (8), we can write the following explicit expressions for the generated state $|\widetilde{\mathrm{LC}}_6\rangle$ by differently factoring the terms referring to the three considered DOFs:

$$\begin{aligned}|\widetilde{\mathrm{LC}}_6\rangle &= \tfrac{1}{2}[|EE\rangle|\phi^+\rangle_\pi|r\ell\rangle + |EE\rangle|\phi^-\rangle_\pi|\ell r\rangle \\ &\quad + |II\rangle|\psi^+\rangle_\pi|r\ell\rangle - |II\rangle|\psi^-\rangle_\pi|\ell r\rangle] \qquad (9a) \\ &= \tfrac{1}{2}[|EE\rangle|HH\rangle|\psi^+\rangle_{\mathbf{k}} + |EE\rangle|VV\rangle|\psi^-\rangle_{\mathbf{k}} \\ &\quad + |II\rangle|VH\rangle|\psi^+\rangle_{\mathbf{k}} + |II\rangle|HV\rangle|\psi^-\rangle_{\mathbf{k}}] \qquad (9b) \\ &= \tfrac{1}{2}[|\phi^+\rangle_c|++\rangle|r\ell\rangle + |\phi^-\rangle_c|--\rangle|r\ell\rangle \\ &\quad + |\phi^+\rangle_c|+-\rangle|\ell r\rangle + |\phi^-\rangle_c|-+\rangle|\ell r\rangle], \qquad (9c)\end{aligned}$$

where we omitted the subscripts AB. The states $|\phi^\pm\rangle_\pi = \frac{1}{\sqrt{2}}(|HH\rangle_{AB} \pm |VV\rangle_{AB})$ and $|\psi^\pm\rangle_\pi = \frac{1}{\sqrt{2}}(|HV\rangle_{AB} \pm |VH\rangle_{AB})$ are the four polarization Bell states, while the states $|\psi^\pm\rangle_{\mathbf{k}}$ and $|\phi^\pm\rangle_c$ are the standard Bell states encoded in the r/ℓ and E/I DOFs, respectively (the "c" subscript standing for "cone").

The realization of the two-qubit gates responsible for the transformation of the hyperentangled state $|\widetilde{\mathrm{HE}}_6\rangle$ into the cluster state $|\widetilde{\mathrm{LC}}_6\rangle$ in terms of optical components was made possible by the insertion of two wave plates after the holed mask; since qubits 1 and 2 belong to photon A, the first CX_{12} gate was realized by means of a $\lambda/2$ wave plate oriented at 45° and intercepting the two internal A modes [see Fig. 2(b) and Eq. (6a)]. Analogously, the CZ_{65} gate was obtained thanks to a second $\lambda/2$ wave plate oriented at 0° and intercepting the two left B modes [see Fig. 2(b) and Eq. (6f)]. It actually proved convenient to have two separated $\lambda/2$ wave plates on the left B modes, but this was a choice uniquely related to our specific experimental setup.

III. CHARACTERIZATION OF THE SIX-QUBIT CLUSTER STATE

We refer now to Fig. 2(c). The two chained interferometers, whose core elements are the three symmetric beam splitters BS_1, BS_{2A}, and BS_{2B}, allow the simultaneous measurement of the three single-qubit compatible observables associated to particles A and B. The r modes are made indistinguishable (in space as well as in time) from the ℓ ones on BS_1, while E and I modes are matched on BS_{2A} or BS_{2B} depending on which photon they refer to. By means of a trombone mirror assembly in each of the two interferometers, it is possible to act on the optical path delays, Δx_1 and Δx_2, and find the optimal temporal superposition conditions for both of the interference phenomena. We now refer to the BS_1: We set $\{|\ell\rangle_j, |r\rangle_j\}$ and $\{|\ell'\rangle_j, |r'\rangle_j\}$, for $j = A, B$, as its input and output states. The insertion of a thin glass plate intercepting two right A modes (one internal and one external) transforms the input states in the following way: $|\phi_A\rangle_{\mathbf{k}} = \frac{1}{\sqrt{2}}(|\ell\rangle_A + e^{-i\phi_A}|r\rangle_A) \to |\ell'\rangle_A$ and $|\phi_A^\perp\rangle_{\mathbf{k}} = \frac{1}{\sqrt{2}}(|\ell\rangle_A - e^{-i\phi_A}|r\rangle_A) \to |r'\rangle_A$ for external and internal modes, respectively. By detecting the photons on the $|\ell'\rangle$ or $|r'\rangle$ output we are projecting the input state respectively into $|\phi_A\rangle$ or $|\phi_A^\perp\rangle$. An analogous glass plate intercepts the left B modes.[1]

Two more such phase shifters, intercepting the external A and B modes, are inserted in the second interferometer before BS_{2A} and BS_{2B}. Four single-photon detectors D_{1A}, D_{2A}, D_{1B}, and D_{2B} receive the radiation belonging to the "up" and "down" output modes [see Fig. 2(b)], which we can

[1] In this case the projection is performed into the states $|\phi_B\rangle_{\mathbf{k}} = \frac{1}{\sqrt{2}}(e^{-i\phi_B}|\ell\rangle_B + |r\rangle_B)$ and $|\phi_B^\perp\rangle_{\mathbf{k}} = \frac{1}{\sqrt{2}}(e^{-i\phi_B}|\ell\rangle_B - |r\rangle_B)$.

label as $\{|E'\rangle_j, |I'\rangle_j\}$ for $j = A, B$. In the presence of the glass plates cited previously, the following input-output transformations concerning BS_{2A} and BS_{2B} hold: $|\delta\rangle_c = \frac{1}{\sqrt{2}}(e^{-i\delta}|E\rangle_j + |I\rangle_j) \rightarrow |E'\rangle_j$ and $|\delta^{\perp}\rangle_c = \frac{1}{\sqrt{2}}(e^{-i\delta}|E\rangle_j - |I\rangle_j) \rightarrow |I'\rangle_j$. Finally, a polarization analyzer constituted of a $\lambda/2$ wave plate, a $\lambda/4$ wave plate, and a polarizing beam splitter (PBS) is added in front of each detector. Under these conditions we recorded nearly 500 coincidences per second.

The characterization of the generated state $|\widetilde{LC}_6\rangle$ relies on a tomographic reconstruction technique followed by a "maximum likelihood" method [30]. Particularly, we aim at recovering Eq. (9), which shows three alternative and perfectly equivalent ways of writing the cluster state $|\widetilde{LC}_6\rangle$. Indeed, Eq. (9) is important to prove since it highlights the inner structure of the generated state. As we see, each of the expressions (9) is obtained by writing the states of four qubits corresponding to two DOFs in a separable basis, and expressing the remaining couple of qubits in the appropriate entangled Bell basis; for example, the first relation shows the four polarization Bell states. Equation (9a) shows that the state $|\widetilde{LC}_6\rangle$ is obtained by a coherent superposition between four terms, each of them referring to a specific pair of correlated modes. We first demonstrated that the four polarization states corresponding to the different pairs of modes are given by the Bell states. The coherence between them can be shown by using Eqs. (9b) and (9c). It is easy to show that the first two terms in (9b) arise from the superposition between the first two terms in (9a), and the same applies for the last two terms. By selecting the appropriate separable basis in two DOFs we performed the tomographic reconstructions to recover the Bell states encoded in the remaining degree of freedom. As a consequence, these measurements prove not only the presence of the various terms appearing in Eq. (9), but also implicitly tell us about the coherences between the states involved.

The reconstruction concerning the polarization variable exactly followed the strategy presented in [30], while the complete sets of tomographic analysis states associated to the two longitudinal momentum DOFs were established combining the known complete set of polarization states (as given in [30]) with the stated correspondence between physical and computational qubits [see Eqs. (6)].

The experimental density matrix reconstructions are shown in Fig. 3 for the polarization variable, in Fig. 4 for the linear momentum **k**, and in Fig. 5 for the E/I DOF. The fidelities associated to the considered tomographic analysis are listed in Table I. As we see, most of these values exceed 80% and some get above 90%; the lowest experimental fidelity corresponds to the tomographic reconstruction associated to the E/I DOF.

We attribute this to the difficulty to achieve perfect mode matching in the second interferometer due to mode divergences and to imperfections of the first interferometer that affect the measurement on the second momentum. Nevertheless, the obtained results represent a first evidence of the correct generation of the cluster state $|\widetilde{LC}_6\rangle$.

As said, the reported tomographic reconstructions allow us to test the validity of Eq. (9); this approach is naturally connected to the first definition of cluster states recalled in this article [see Eq. (2)].

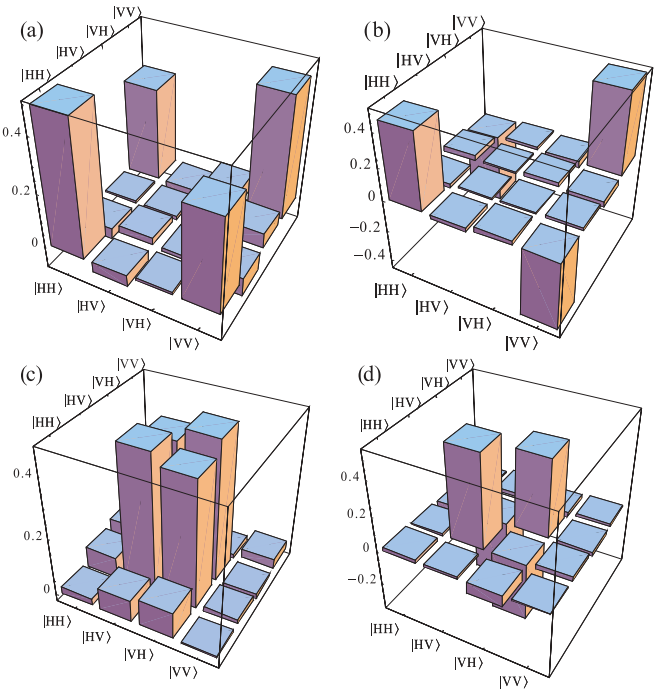

FIG. 3. (Color online) Tomographic reconstruction of the four polarization states in Eq. (9) (real parts). The imaginary components are negligible. The corresponding theoretical Bell states are: (a) $|\phi^+\rangle_\pi$, (b) $|\phi^-\rangle_\pi$, (c) $|\psi^+\rangle_\pi$, (d) $|\psi^-\rangle_\pi$.

Furthermore, we completely characterized the generated cluster state in terms of its stabilizing operators: Their experimental expectation values $\{\langle \widetilde{S}_j \rangle\}_{j=1}^{64}$ are shown in Table II. From these values we calculated the fidelity of the generated state $F_{|\widetilde{LC}_6\rangle} = 0.6350 \pm 0.0008$ and an entanglement witness $\langle \mathcal{W}_F \rangle = -0.270 \pm 0.002$, which proves the existence of a

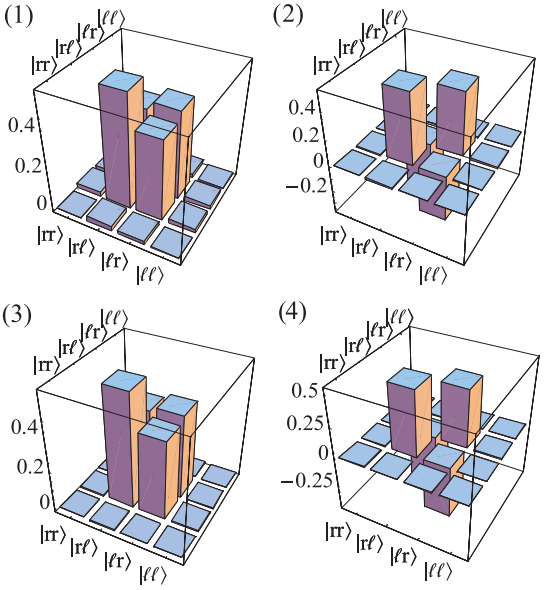

FIG. 4. (Color online) Tomographic reconstruction of the four states encoded in the r/ℓ DOF (real parts). The imaginary components are negligible. The corresponding theoretical Bell states are: (1) and (3) $|\psi^+\rangle_{\mathbf{k}}$, (2) and (4) $|\psi^-\rangle_{\mathbf{k}}$.

TABLE I. Fidelities of Bell states for each DOF. We selected a separable state for two DOFs (leftmost column) and performed a tomographic reconstruction of the density matrix of the remaining DOF (next column). The expected output states and the relative fidelities are shown in the remaining two columns.

Separable basis	Output DOF	Output state	Fidelity
$\|EE\rangle_c\|r\ell\rangle_{\mathbf{k}}$	π	$\|\phi^+\rangle_\pi$	0.821 ± 0.014
$\|EE\rangle_c\|\ell r\rangle_{\mathbf{k}}$		$\|\phi^-\rangle_\pi$	0.917 ± 0.017
$\|II\rangle_c\|r\ell\rangle_{\mathbf{k}}$		$\|\psi^+\rangle_\pi$	0.905 ± 0.013
$\|II\rangle_c\|\ell r\rangle_{\mathbf{k}}$		$\|\psi^-\rangle_\pi$	0.828 ± 0.025
$\|EE\rangle_c\|HH\rangle_\pi$	r/ℓ	$\|\psi^+\rangle_{\mathbf{k}}$	0.897 ± 0.008
$\|EE\rangle_c\|VV\rangle_\pi$		$\|\psi^-\rangle_{\mathbf{k}}$	0.933 ± 0.016
$\|II\rangle_c\|VH\rangle_\pi$		$\|\psi^+\rangle_{\mathbf{k}}$	0.899 ± 0.009
$\|II\rangle_c\|HV\rangle_\pi$		$\|\psi^-\rangle_{\mathbf{k}}$	0.858 ± 0.017
$\|{+}{+}\rangle_\pi\|r\ell\rangle_{\mathbf{k}}$	E/I	$\|\phi^+\rangle_c$	0.797 ± 0.015

TABLE II. Experimental results: measurement of the 64 stabilizers $\widetilde{S}_i$ of $|\widetilde{\mathrm{LC}_6}\rangle$, that is, all the products of the generators $\widetilde{g}_i$. In the second column we report the explicit form of the stabilizers written in terms of the Pauli matrices.

Stabilizer	Operator	Experimental value
1	$\mathbb{1}$	1.0000 ± 0.0000
$\tilde{g}_1$	$X_1X_2X_4$	0.5928 ± 0.0075
$\tilde{g}_2$	$Z_1Z_2Z_5$	0.8788 ± 0.0053
$\tilde{g}_3$	$-Z_3Z_6$	0.9984 ± 0.0005
$\tilde{g}_4$	Z_1Z_4	0.9973 ± 0.0008
$\tilde{g}_5$	$-X_2X_5Z_6$	0.7905 ± 0.0057
$\tilde{g}_6$	$X_3Z_5X_6$	0.8310 ± 0.0062
$\tilde{g}_1\tilde{g}_2$	$-Y_1Y_2X_4Z_5$	0.5657 ± 0.0059
$\tilde{g}_1\tilde{g}_3$	$-X_1X_2Z_3X_4Z_6$	0.5930 ± 0.0075
$\tilde{g}_1\tilde{g}_4$	$-Y_1Y_2Y_4$	0.5602 ± 0.0076
$\tilde{g}_1\tilde{g}_5$	$-X_1X_4X_5Z_6$	0.5872 ± 0.0076
$\tilde{g}_1\tilde{g}_6$	$X_1X_2X_3X_4Z_5X_6$	0.4653 ± 0.0095
$\tilde{g}_2\tilde{g}_3$	$-Z_1Z_2Z_3Z_5Z_6$	0.8586 ± 0.0062
$\tilde{g}_2\tilde{g}_4$	$Z_2Z_4Z_5$	0.8775 ± 0.0053
$\tilde{g}_2\tilde{g}_5$	$Z_1Y_2Y_5Z_6$	0.7042 ± 00066
$\tilde{g}_2\tilde{g}_6$	$Z_1Z_2X_3X_6$	0.8288 ± 0.0062
$\tilde{g}_3\tilde{g}_4$	$-Z_1Z_3Z_4Z_6$	0.9970 ± 0.0009
$\tilde{g}_3\tilde{g}_5$	$X_2Z_3X_5$	0.7896 ± 0.0057
$\tilde{g}_3\tilde{g}_6$	$Y_3Z_5Y_6$	0.7484 ± 0.0056
$\tilde{g}_4\tilde{g}_5$	$-Z_1X_2Z_4X_5Z_6$	0.7339 ± 0.0084
$\tilde{g}_4\tilde{g}_6$	$Z_1X_3Z_4Z_5X_6$	0.8312 ± 0.0062
$\tilde{g}_5\tilde{g}_6$	$-X_2X_3Y_5Y_6$	0.6392 ± 0.0060
$\tilde{g}_1\tilde{g}_2\tilde{g}_3$	$Y_1Y_2Z_3X_4Z_5Z_6$	0.4504 ± 0.0092
$\tilde{g}_1\tilde{g}_2\tilde{g}_4$	$-X_1Y_2Y_4Z_5$	0.6063 ± 0.0074
$\tilde{g}_1\tilde{g}_2\tilde{g}_5$	$Y_1Z_2X_4Y_5Z_6$	0.5378 ± 0.0086
$\tilde{g}_1\tilde{g}_2\tilde{g}_6$	$-Y_1Y_2X_3X_4X_6$	0.4169 ± 0.0065
$\tilde{g}_1\tilde{g}_3\tilde{g}_4$	$Y_1X_2Z_3Y_4Z_6$	0.5603 ± 0.0076
$\tilde{g}_1\tilde{g}_3\tilde{g}_5$	$X_1Z_3X_4X_5$	0.5874 ± 0.0075
$\tilde{g}_1\tilde{g}_3\tilde{g}_6$	$X_1X_2Y_3X_4Z_5Y_6$	0.4651 ± 0.0063
$\tilde{g}_1\tilde{g}_4\tilde{g}_5$	$Y_1Y_4X_5Z_6$	0.5882 ± 0.0074
$\tilde{g}_1\tilde{g}_4\tilde{g}_6$	$-Y_1X_2X_3Y_4Z_5X_6$	0.4148 ± 0.0075
$\tilde{g}_1\tilde{g}_5\tilde{g}_6$	$-X_1X_3X_4Y_5Y_6$	0.4450 ± 0.0061
$\tilde{g}_2\tilde{g}_3\tilde{g}_4$	$-Z_2Z_3Z_4Z_5Z_6$	0.8592 ± 0.0062
$\tilde{g}_2\tilde{g}_3\tilde{g}_5$	$-Z_1Y_2Z_3Y_5$	0.7036 ± 0.0066

TABLE II. (*Continued.*)

Stabilizer	Operator	Experimental value
$\tilde{g}_2\tilde{g}_3\tilde{g}_6$	$Z_1Z_2Y_3Y_6$	0.7468 ± 0.0056
$\tilde{g}_2\tilde{g}_4\tilde{g}_5$	$Y_2Z_4Y_5Z_6$	0.7038 ± 0.0066
$\tilde{g}_2\tilde{g}_4\tilde{g}_6$	$Z_2X_3Z_4X_6$	0.8285 ± 0.0062
$\tilde{g}_2\tilde{g}_5\tilde{g}_6$	$-Z_1Y_2X_3X_5Y_6$	0.6861 ± 0.0058
$\tilde{g}_3\tilde{g}_4\tilde{g}_5$	$Z_1X_2Z_3Z_4X_5$	0.7357 ± 0.0083
$\tilde{g}_3\tilde{g}_4\tilde{g}_6$	$Z_1Y_3Z_4Z_5Y_6$	0.7484 ± 0.0056
$\tilde{g}_3\tilde{g}_5\tilde{g}_6$	$X_2Y_3Y_5X_6$	0.6625 ± 0.0051
$\tilde{g}_4\tilde{g}_5\tilde{g}_6$	$-Z_1X_2X_3Z_4Y_5Y_6$	0.6394 ± 0.0060
$\tilde{g}_1\tilde{g}_2\tilde{g}_3\tilde{g}_4$	$X_1Y_2Z_3Y_4Z_5Z_6$	0.6067 ± 0.0074
$\tilde{g}_1\tilde{g}_2\tilde{g}_3\tilde{g}_5$	$-Y_1Z_2Z_3X_4Y_5$	0.5391 ± 0.0086
$\tilde{g}_1\tilde{g}_2\tilde{g}_3\tilde{g}_6$	$-Y_1Y_2Y_3X_4Y_6$	0.4334 ± 0.0063
$\tilde{g}_1\tilde{g}_2\tilde{g}_4\tilde{g}_5$	$X_1Z_2Y_4Y_5Z_6$	0.4247 ± 0.0093
$\tilde{g}_1\tilde{g}_2\tilde{g}_4\tilde{g}_6$	$-X_1Y_2X_3Y_4X_6$	0.3960 ± 0.0077
$\tilde{g}_1\tilde{g}_2\tilde{g}_5\tilde{g}_6$	$-Y_1Z_2X_3X_4X_5Y_6$	0.4435 ± 0.0076
$\tilde{g}_1\tilde{g}_3\tilde{g}_4\tilde{g}_5$	$-Y_1Z_3Y_4X_5$	0.5897 ± 0.0074
$\tilde{g}_1\tilde{g}_3\tilde{g}_4\tilde{g}_6$	$-Y_1X_2Y_3Y_4Z_5Y_6$	0.4349 ± 0.0080
$\tilde{g}_1\tilde{g}_3\tilde{g}_5\tilde{g}_6$	$X_1Y_3X_4Y_5X_6$	0.4465 ± 0.0061
$\tilde{g}_1\tilde{g}_4\tilde{g}_5\tilde{g}_6$	$Y_1X_3Y_4Y_5Y_6$	0.4465 ± 0.0061
$\tilde{g}_2\tilde{g}_3\tilde{g}_4\tilde{g}_5$	$-Y_2Z_3Z_4Y_5$	0.7037 ± 0.0066
$\tilde{g}_2\tilde{g}_3\tilde{g}_4\tilde{g}_6$	$Z_2Y_3Z_4Y_6$	0.7465 ± 0.0056
$\tilde{g}_2\tilde{g}_3\tilde{g}_5\tilde{g}_6$	$Z1Y2Y3X5X6$	0.6113 ± 0.0063
$\tilde{g}_2\tilde{g}_4\tilde{g}_5\tilde{g}_6$	$-Y_2X_3Z_4X_5Y_6$	0.6860 ± 0.0058
$\tilde{g}_3\tilde{g}_4\tilde{g}_5\tilde{g}_6$	$Z_1X_2Y_3Z_4Y_5X_6$	0.6624 ± 0.0051
$\tilde{g}_1\tilde{g}_2\tilde{g}_3\tilde{g}_4\tilde{g}_5$	$-X_1Z_2Z_3Y_4Y_5$	0.4235 ± 0.0093
$\tilde{g}_1\tilde{g}_2\tilde{g}_3\tilde{g}_4\tilde{g}_6$	$-X_1Y_2Y_3Y_4Y_6$	0.3735 ± 0.0078
$\tilde{g}_1\tilde{g}_2\tilde{g}_3\tilde{g}_5\tilde{g}_6$	$Y_1Z_2Y_3X_4X_5X_6$	0.4071 ± 0.0077
$\tilde{g}_1\tilde{g}_2\tilde{g}_4\tilde{g}_5\tilde{g}_6$	$-X_1Z_2X_3Y_4X_5Y_6$	0.5059 ± 0.0052
$\tilde{g}_1\tilde{g}_3\tilde{g}_4\tilde{g}_5\tilde{g}_6$	$-Y_1Y_3Y_4Y_5X_6$	0.4884 ± 0.0057
$\tilde{g}_2\tilde{g}_3\tilde{g}_4\tilde{g}_5\tilde{g}_6$	$Y_2Y_3Z_4X_5X_6$	0.6112 ± 0.0063
$\tilde{g}_1\tilde{g}_2\tilde{g}_3\tilde{g}_4\tilde{g}_5\tilde{g}_6$	$X_1Z_2Y_3Y_4X_5X_6$	0.4046 ± 0.0060

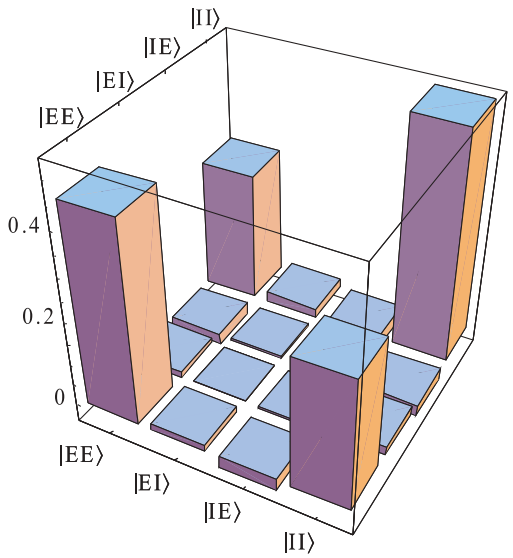

FIG. 5. (Color online) Tomographic reconstruction of the state encoded in the E/I DOF (real part) corresponding to the $r_A - \ell_B$ spatial mode pair and the polarization state $|+\rangle_A|+\rangle_B$. The imaginary components is negligible. The corresponding theoretical state is $|\phi^+\rangle_c$.

genuine six-qubit entanglement (see [29] for details). The fidelity value is limited by imperfections in phase and polarization settings, such as the two controlled operations (CX and CZ), and mainly by nonperfect mode matching on the three beam splitters (BSs), as said. The different values of the measured stabilizers depend on the specific Pauli matrices appearing in their expressions. Precisely, the larger the number of the involved X_j and Y_j Pauli operators, the lower the experimental value of the measured stabilizer. This feature will be important in the discussion of the realized CNOT gate. The data shown in Table II were also used for a nonlocality test of quantum mechanics (see [29] for more details concerning Bell inequalities with the two-photon, six-qubit linear cluster state).

IV. EXPERIMENTAL REALIZATION OF THE CNOT GATE

We now turn to the one-way model of QC [10]. Given a cluster state, it can be useful to think of the distinct horizontal qubits as "the original [logical] qubit at different times" [31], with the temporal axis oriented from left to right (a choice made possible by appropriately designing the lattice); single-qubit gates are represented by pairs of horizontally adjacent qubits, while vertical connections play the role of CPHASE gates. Each computation process is then obtained as a sequence of single-qubit projective measurements performed on the so-called physical qubits, simultaneously determining the propagation of information through the cluster and the loss of entanglement in the original state [6,31].

This last feature is responsible for the irreversibility of the process and explains why we speak of one-way computation. The difference existing between physical and encoded qubits deserves a deeper understanding. Physical qubits in the initial cluster state represent an entanglement resource; encoded (or logical) qubits constitute the quantum information being processed [32]. Let N be the number of physical qubits and M the number of encoded qubits, with $M < N$. M input cluster qubits, all prepared in the state $|+\rangle$, are usually positioned on the left of the two-dimensional graph. The single-qubit measurements involve $N - M$ qubits. Consequently, the output of the computation can be read on the M unmeasured qubits up to local Pauli errors, as is specified later in this paper. More precisely, the measurements driving the computation are performed in the following basis:

$$B_i(\alpha) = \{|\alpha_+\rangle_i, |\alpha_-\rangle_i\}, \tag{10}$$

with $|\alpha_\pm\rangle_i = \frac{1}{\sqrt{2}}(e^{i\alpha/2}|0\rangle_i + e^{-i\alpha/2}|1\rangle_i)$. If we take s_i as signaling the presence of a Pauli error, we usually associate $s_i = 0$ to the measurement outcome $|\alpha_+\rangle$ (error-free case) and $s_i = 1$ to $|\alpha_-\rangle$. The choice of α (and the consequent possible errors occurring in the computation) depends on the algorithm to be implemented. Measuring a qubit in the computational basis $\{|0\rangle_i, |1\rangle_i\}$ has a completely different effect on the cluster in that it removes the measured qubit and leads to the cluster state

$$\prod_{k\in\mathcal{N}_i} Z_k^{s_i} |\Phi_{N-1}^{\mathcal{L}\setminus\{i\}}\rangle, \tag{11}$$

where $\mathcal{N}_i$ is the set of vertices connected to site i.

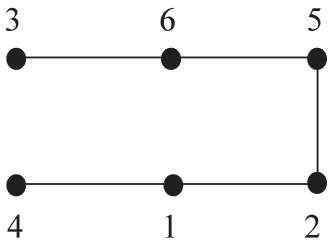

FIG. 6. Graph associated to the six-qubit horseshoe cluster state, equivalent to the generated linear cluster state.

The generated six-qubit cluster allows the implementation of nontrivial two-qubit operations such as the CNOT gate. For this purpose, it is convenient to think of a horseshoe (180° rotated) six-qubit cluster instead of the one depicted in Fig. 1(b); the two are physically equivalent, but the horseshoe one is easier to translate into a circuit representation of the CNOT gate. We now consider Fig. 6. Since we realize our computation within the one-way model, we perform simultaneous single-qubit measurements on qubits 3 and 4 and on qubits 6 and 1 and then read the corresponding output on qubits 5 and 2, both encoded in the polarization DOF.

We pointed out four possible measurement patterns in order to accomplish different logical operations, depending on the bases chosen for the single-qubit measurements. From now on, when referring to a given measurement basis we will always think of the so-called "laboratory basis" (LB), which differs from the "cluster basis" (CB) because of the presence of the local operations affecting qubits 3 ($X_3\mathsf{H}_3$) and 4 (H_4) [see Eq. (8)]. The four considered measurement patterns, both in the cluster and in the laboratory bases, are listed in Table III.

For each pattern a corresponding computational circuit can be derived. In Fig. 7 we show the detailed derivation of the corresponding circuit for the first considered pattern: The measurements implement the "Cluster algorithm" (see figure)

TABLE III. Measurement bases for the different considered patterns. For each pattern we indicate the measured qubit (and the DOF in which the qubit is encoded) and the corresponding measurement in the cluster (CB) and laboratory bases (LB).

Pattern	Qubit [DOF]	Measurement CB	Measurement LB
I	$3[r/\ell]$	$\{\|0\rangle,\|1\rangle\}$	$\{\|+\rangle,\|-\rangle\}$
	$4[E/I]$	$\{\|0\rangle,\|1\rangle\}$	$\{\|+\rangle,\|-\rangle\}$
	$6[r/\ell]$	$B(\alpha)$[a]	$B(\alpha)$[a]
	$1[E/I]$	$B(\beta)$[a]	$B(\beta)$[a]
II	$3[r/\ell]$	$\{\|0\rangle,\|1\rangle\}$	$\{\|+\rangle,\|-\rangle\}$
	$4[E/I]$	$B(0)$	$\{\|0\rangle,\|1\rangle\}$
	$6[r/\ell]$	$B(\alpha)$	$B(\alpha)$
	$1[E/I]$	$B(0)$	$\{\|+\rangle,\|-\rangle\}$
III	$3[r/\ell]$	$B(0)$	$\{\|1\rangle,\|0\rangle\}$
	$4[E/I]$	$\{\|0\rangle,\|1\rangle\}$	$\{\|+\rangle,\|-\rangle\}$
	$6[r/\ell]$	$B(0)$	$\{\|+\rangle,\|-\rangle\}$
	$1[E/I]$	$B(\beta)$	$B(\beta)$
IV	$3[r/\ell]$	$B(0)$	$\{\|1\rangle,\|0\rangle\}$
	$4[E/I]$	$B(0)$	$\{\|0\rangle,\|1\rangle\}$
	$6[r/\ell]$	$B(0)$	$\{\|+\rangle,\|-\rangle\}$
	$1[E/I]$	$B(0)$	$\{\|+\rangle,\|-\rangle\}$

[a]See Eq. (10).

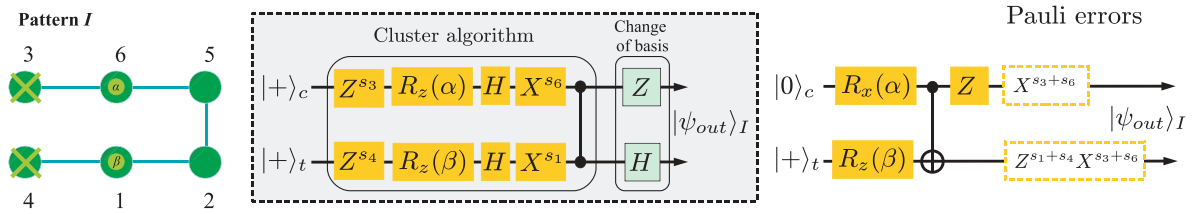

FIG. 7. (Color online) Measurement pattern I. A cross stands for a measurement in the basis $\{|0\rangle,|1\rangle\}$, while α and β indicate a measurement in the bases $B(\alpha)$ and $B(\beta)$. The output state is encoded in qubits 5 and 2. The circuit associated to the considered measurement is shown. We first indicate the circuit obtained by directly following the one-way rules and then the equivalent circuit composed by single-qubit gates and a two-qubit CNOT gate. The gates labeled as "Change of basis" are due to the transformation between the computational and laboratory bases.

and the change between the CB and the LB corresponds to the final gates (labeled as "Change of basis" in the figure). The circuit can be equivalently written as shown in the rightmost section: It consists of two single-qubit rotations and a CNOT gate. The Pauli errors, as usual, depend on the measurement results of qubits 3, 4, 6, and 1. In Fig. 8 we show the equivalent circuits corresponding to the other three measurement patterns we have considered.

By taking into account their circuit representations shown in Fig. 7 and Fig. 8, we can write the expected output state, encoded in the physical qubits 5 (photon B, control) and 2 (photon A, target), for each measurement pattern:

$$|\psi_{\rm out}\rangle_{\rm I} = \left(X_5^{s_3+s_6} Z_2^{s_1+s_4} X_2^{s_3+s_6}\right) \times Z_5{\rm CNOT}_{52}\left[R_x^{(5)}(\alpha)\otimes R_z^{(2)}(\beta)\right]|0\rangle_5|+\rangle_2, \quad (12a)$$

$$|\psi_{\rm out}\rangle_{\rm II} = \left(X_5^{s_3+s_6} X_2^{s_3+s_4+s_6}\right) \times Z_5{\rm CNOT}_{52}\left[R_x^{(5)}(\alpha)\otimes \mathbb{1}_2\right]|0\rangle_5|0\rangle_2, \quad (12b)$$

$$|\psi_{\rm out}\rangle_{\rm III} = \left(Z_5^{s_3} Z_2^{s_1+s_4}\right) \times Z_5{\rm CNOT}_{52}\left[\mathbb{1}_5\otimes R_z^{(2)}(\beta)\right]|+\rangle_5|+\rangle_2, \quad (12c)$$

$$|\psi_{\rm out}\rangle_{\rm IV} = \left(Z_B^{s_3} X_A^{s_4}\right) Z_5{\rm CNOT}_{52}|+\rangle_5|0\rangle_2, \quad (12d)$$

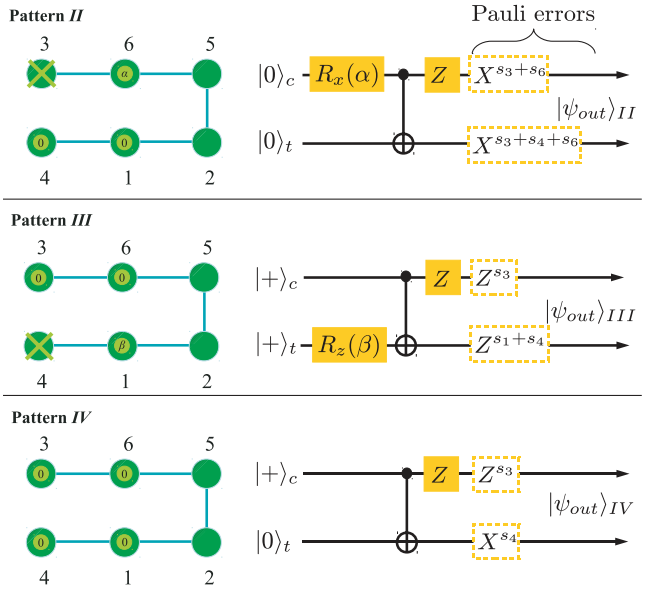

FIG. 8. (Color online) Measurement patterns II, III, and IV and the corresponding circuit representations. Each circuit is composed by single-qubit gates and a two-qubit CNOT gate.

where $R_x(\alpha) = e^{-i\alpha X/2}$ corresponds to a counterclockwise rotation through an angle α about the x axis of the Bloch sphere [an analogous definition holds for $R_z(\beta)$]. The presence of the single-qubit Pauli errors X and Z depends on the measurement output of the corresponding qubit [represented by s_i for $i = 1,3,4,6$; see the comment following Eq. (10)]. It comes out from the expressions of $|\psi_{\rm out}\rangle$ in (12) that the computations can be interpreted as single-qubit transformations followed by a CNOT gate acting on different input states. Precisely, by rewriting the computation in the error-free case we obtain

$$|\psi_{\rm out}\rangle_{\rm I} = Z_5{\rm CNOT}_{52}\left[R_x^{(5)}(\alpha)\otimes R_z^{(2)}(\beta)\right]|\psi_{\rm in}\rangle_{\rm I}, \quad (13a)$$

$$|\psi_{\rm out}\rangle_{\rm II} = Z_5{\rm CNOT}_{52}\left[R_x^{(5)}(\alpha)\otimes \mathbb{1}_2\right]|\psi_{\rm in}\rangle_{\rm II}, \quad (13b)$$

$$|\psi_{\rm out}\rangle_{\rm III} = Z_5{\rm CNOT}_{52}\left[\mathbb{1}_5\otimes R_z^{(2)}(\beta)\right]|\psi_{\rm in}\rangle_{\rm III}, \quad (13c)$$

$$|\psi_{\rm out}\rangle_{\rm IV} = Z_5{\rm CNOT}_{52}|\psi_{\rm in}\rangle_{\rm IV}, \quad (13d)$$

where the input states are $|\psi_{\rm in}\rangle_{\rm I} = |0\rangle_5|+\rangle_2$, $|\psi_{\rm in}\rangle_{\rm II} = |0\rangle_5|0\rangle_2$, $|\psi_{\rm in}\rangle_{\rm III} = |+\rangle_5|+\rangle_2$, and $|\psi_{\rm in}\rangle_{\rm IV} = |+\rangle_5|0\rangle_2$.

We start from pattern IV: In this case, by looking at the measurement basis given in Table III, it is possible to reinterpret the four tomographic reconstructions of the cluster state $|\widetilde{\rm LC}_6\rangle$ with respect to the polarization DOF as a one-way computation (here the CNOT operation). Precisely, the measurement of qubits 3 and 4 in the computational basis corresponds to selecting different modes of the cluster. The output is then encoded in the polarization of the two photons and the four Bell states correspond to the four different outputs of the computation. In fact, it is easy to show that $|\psi_{\rm out}\rangle_{\rm IV} = |\phi^-\rangle_{52}$ in the error-free case. The other three Bell states are obtained by applying the different Pauli errors. Hence, the tomographic reconstructions of the polarization states given in Sec. III suffice to the experimental proof of the correct functioning of the realized logic gate within the specific framework of pattern IV.

We then consider patterns I, II, and III in the error-free case, which means that $s_i = 0$ for $i = 1,3,4,6$. Moreover, we set $\alpha = \beta = 0$, implying that $R_x(0) = R_z(0) = \mathbb{1}$. These hypotheses lead to the output states $|\psi_{\rm out}\rangle_{\rm I}$, $|\psi_{\rm out}\rangle_{\rm II}$, and $|\psi_{\rm out}\rangle_{\rm III}$, all in the form of separable states of the two photons A and B, and establish a first set of input and output states for the three cases. Under these conditions, it is interesting to reconstruct the input-output (I-O) matrices for the realized CNOT gate, the knowledge of which makes possible the further calculation of the fidelities associated to the output states (13a)–(13c). The experimental results are listed in Table IV, while Fig. 9 shows a

TABLE IV. Input-output states, corresponding to the first three measurement patterns, expressed in the polarization basis. Here the "AB" ordering is used.

Pattern	Input state	Expected output state	Fidelity
I	$\|+H\rangle_{AB}$	$\|+H\rangle_{AB}$	0.6052 ± 0.0084
	$\|-H\rangle_{AB}$	$\|-H\rangle_{AB}$	0.6657 ± 0.0077
	$\|-V\rangle_{AB}$	$\|-V\rangle_{AB}$	0.5476 ± 0.0066
	$\|+V\rangle_{AB}$	$\|+V\rangle_{AB}$	0.6223 ± 0.0069
II	$\|HH\rangle_{AB}$	$\|HH\rangle_{AB}$	0.8716 ± 0.0050
	$\|VH\rangle_{AB}$	$\|VH\rangle_{AB}$	0.8348 ± 0.0072
	$\|HV\rangle_{AB}$	$\|VV\rangle_{AB}$	0.8710 ± 0.0053
	$\|VV\rangle_{AB}$	$\|HV\rangle_{AB}$	0.8376 ± 0.0065
III	$\|++\rangle_{AB}$	$\|+-\rangle_{AB}$	0.6541 ± 0.0111
	$\|+-\rangle_{AB}$	$\|++\rangle_{AB}$	0.6798 ± 0.0088
	$\|--\rangle_{AB}$	$\|--\rangle_{AB}$	0.6741 ± 0.0108
	$\|-+\rangle_{AB}$	$\|-+\rangle_{AB}$	0.6096 ± 0.0093

graphic representation of the I-O matrices. The fidelity values show that the gate built on the generated cluster state $|\widetilde{\mathrm{LC}}_6\rangle$ operates as expected.

A further analysis consists of examining other possible values for the rotation angles α and β in the framework of an error-free computation. By letting α and β assume nonzero values during the computation, we obtain other combinations of input and output product states. As an example, we consider

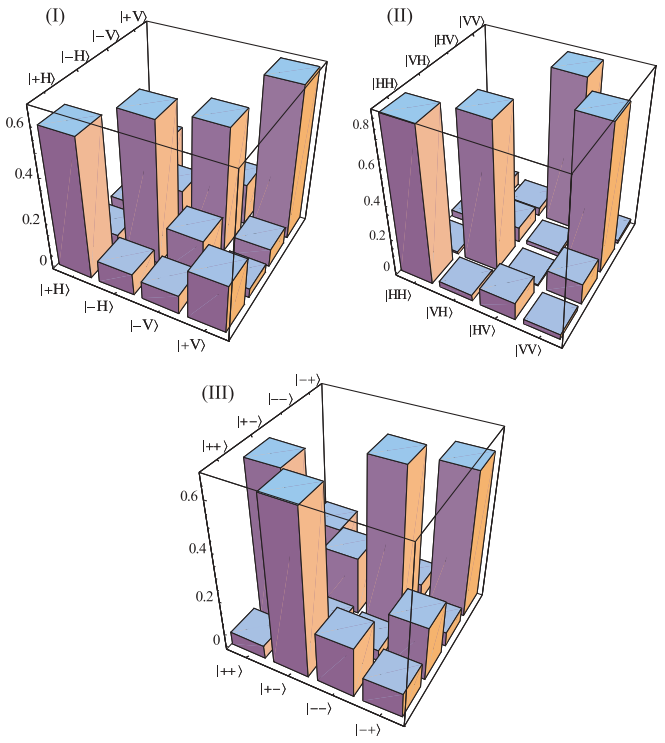

FIG. 9. (Color online) Graphic representation of the I-O matrices for the considered CNOT operation. The sublabels indicate the pattern to which each matrix refers. The sets of input and output states are listed in Table IV and can be read on the upper (input) and lower (output) axis.

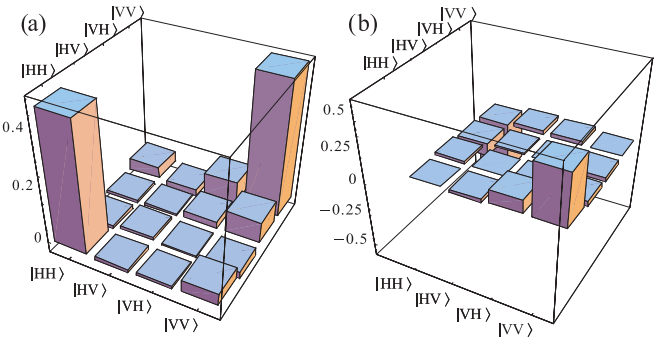

FIG. 10. (Color online) Tomographic reconstruction of the polarization entangled output state $|\psi'_{\mathrm{out}}\rangle_{\mathrm{II}}$. Both the (a) real and (b) imaginary components are shown. The corresponding theoretical state is $-\frac{1}{\sqrt{2}}(|HH\rangle_{AB} - i|VV\rangle_{AB})$.

the "variant" of pattern II, where $\alpha = 3\pi/2$. We can then write the output state as

$$|\psi'_{\mathrm{out}}\rangle_{\mathrm{II}} = Z_5 \mathrm{CNOT}_{52} R_x^{(5)}(3\pi/2)|0\rangle_5|0\rangle_2 = -\frac{1}{\sqrt{2}}(|HH\rangle_{AB} - i|VV\rangle_{AB}). \quad (14)$$

As we see, here we have an entangled two-photon state encoded in polarization. When dealing with an entangled state of photons A and B it is not possible to adopt an I-O matrix reconstruction strategy in order to test the correctness of the gate's functioning; it is now necessary to perform a tomographic reconstruction of the output state corresponding to the considered computation (this is exactly what happens with case IV, too). The experimental tomographic analysis for the "case II variant" is shown in Fig. 10: The fidelity of the output state $|\psi'_{\mathrm{out}}\rangle_{\mathrm{II}}$ is $F = 0.879 \pm 0.017$.

We now comment on the latter fidelity (a similar observation holds for the fidelities given in Table IV for pattern II. Its value (87.9%) is larger than the fidelity of the cluster state (63.5%). This apparent discrepancy resides on the considered measurement pattern. Precisely, it is the measurement basis chosen in this case for qubits 1 and 4 (the ones encoded in the E/I momentum) that distinguishes pattern II from the others. Indeed, Table I shows that the E/I DOF is mainly responsible for the limited value of the generated cluster state fidelity. However, in pattern II the measurement basis for qubit 4 is $\{|0\rangle,|1\rangle\}$ (see Table III). In this basis the visibility is almost perfect, as it is possible to see from the expectation value of $\widetilde{g}_4$ in Table II. As a consequence, even if the cluster state has an overall fidelity of 63.5%, depending on the particular choice of the measurement pattern, it is still possible that the fidelity of the output of the considered computation is larger than the overall state fidelity.

V. CONCLUSIONS AND PERSPECTIVES

We have characterized the six-qubit linear cluster state $|\widetilde{\mathrm{LC}}_6\rangle$, realized by starting from a two-photon state, hyperentangled in the three DOFs of polarization and a double set of longitudinal momentum modes of the photons emitted over the degenerate cone of a Type I SPDC crystal.

The importance of a six-qubit linear cluster state is twofold: while it represents a significant step in the research of quantum nonlocality, as recently demonstrated [29], the realization of cluster states with an increasing number of qubits is important to the QC community. Indeed, we have used this state by realizing the CNOT gate in the one-way QC domain. For this purpose, the configuration chosen for the graph associated to the six-qubit state is that of a horseshoe (180° rotated) cluster state.

The CNOT results of our experiment are similar to those obtained within the Hefei group experiment [33], where a six-qubit graph state was created by using polarization and spatial modes of four photons. By that technique new qubits encoded in different DOFs of the same photon are added by local operations. Multiqubit entangled states realized by this technique may find useful applications in one-way QC.

Both the existing approaches to one-way QC and error encoding, based on multiphoton and multi-DOF entanglement, contribute to make an all-optical architecture a serious contender for the ultimate goal of a large-scale quantum computer. However, scalable linear optics systems are required for the realization of more complex QC operations and algorithms. This is a very challenging objective, according to the current optical technology. One of the main reasons is that an increasing number of qubits requires the setup of bulk measurement systems of increasing complexity. At the same time, the need for an increasing number of qubits in a QC algorithm conflicts with the intrinsic limitations of the SPDC process. Indeed, no more than few pairs of photons at a time are created by SPDC, due to its probabilistic nature. Moreover, multiphoton detection is seriously affected by the limited quantum efficiencies of modern detectors.

In order to take the maximum advantage of the possibilities offered by the current optical technology to increase power and speed of computational operations based on high-dimension entangled photonic systems, we may conceive cluster states built on a number of photons entangled in many DOFs. Increasing the number of photons or encoding the qubits in other DOFs of the particles, besides polarization [34] and longitudinal momentum [35], such as frequency [36], time bin [37], and orbital angular momentum of the photons [38], are two complementary (but not exclusive) approaches to enhancing the computational power and the information content.

It is worth remembering that increasing the number n of involved DOFs implies an exponential requirement of resources. For instance, 2^n **k** modes per photon must be selected within the emission cone to encode n qubits in each photon. However, according to the current optical technology, working with few DOFs (such as $n = 2,3,4$) offers still more advantages than working with a corresponding number of photon pairs, because of the higher repetition rate and state generation and detection efficiency. Indeed, by increasing the number of DOFs on which two photons are entangled, the overall detection efficiency and hence the repetition rate of detection is constant, since it scales as η^N, N being the number of photons and η the detector quantum efficiency, except for some factors depending on the measurement setup. Furthermore, an entangled state built on a larger number of particles is in principle more affected by decoherence because of the increased difficulty of making photons indistinguishable. On a medium-term time scale a hybrid approach to QC (i.e., multi-DOF and multiphoton states) may represent a convenient solution to overcoming the structural limitations in generation and detection of quantum photon states.

In view of an efficient linear optics QC, the use of miniaturized optical circuits built on a chip in the realization of increasingly complex linear optical schemes consisting of many interferometers, whose feasibility has been recently demonstrated [39–42], is becoming of fundamental relevance. Indeed, these new integrated structures guarantee high fidelities and highly intrinsic phase stability of the measurements necessary to perform the logical operations. Furthermore, the adoption of integrated optics may also enable the realization of novel kinds of multiphoton states. Hence, new exciting perspectives implying the solution of new problems are opened in the application of miniaturized optical structures with multiphoton multi-DOF entangled states.

[1] M. Hein, J. Eisert, and H. J. Briegel, Phys. Rev. A **69**, 062311 (2004).

[2] N. D. Mermin, Phys. Rev. Lett. **65**, 1838 (1990).

[3] O. Gühne, G. Tóth, P. Hyllus, and H. J. Briegel, Phys. Rev. Lett. **95**, 120405 (2005).

[4] A. Cabello and P. Moreno, Phys. Rev. Lett. **99**, 220402 (2007).

[5] A. Cabello, O. Gühne, and D. Rodríguez, Phys. Rev. A **77**, 062106 (2008).

[6] R. Raussendorf and H. J. Briegel, Phys. Rev. Lett. **86**, 5188 (2001).

[7] H. J. Briegel and R. Raussendorf, Phys. Rev. Lett. **86**, 910 (2001).

[8] R. Cleve, D. Gottesman, and H.-K. Lo, Phys. Rev. Lett. **83**, 648 (1999).

[9] D. Schlingemann and R. F. Werner, Phys. Rev. A **65**, 012308 (2001).

[10] H. J. Briegel, D. E. Browne, W. Dür, R. Raussendorf, and M. V. den Nest, Nat. Phys. **5**, 19 (2009).

[11] K. Chen, C.-M. Li, Q. Zhang, Y.-A. Chen, A. Goebel, S. Chen, A. Mair, and J.-W. Pan, Phys. Rev. Lett. **99**, 120503 (2007).

[12] G. Vallone, E. Pomarico, F. De Martini, and P. Mataloni, Phys. Rev. Lett. **100**, 160502 (2008).

[13] Z. Zhao, T. Yang, Y.-A. Chen, A.-N. Zhang, M. Żukowski, and J.-W. Pan, Phys. Rev. Lett. **91**, 180401 (2003).

[14] P. Walther, K. J. Resch, T. Rudolph, E. Schenck, H. Weinfurter, V. Vedral, M. Aspelmeyer, and A. Zeilinger, Nature (London) **434**, 169 (2005).

[15] P. Walther, M. Aspelmeyer, K. J. Resch, and A. Zeilinger, Phys. Rev. Lett. **95**, 020403 (2005).

[16] N. Kiesel, C. Schmid, U. Weber, G. Tóth, O. Gühne, R. Ursin, and H. Weinfurter, Phys. Rev. Lett. **95**, 210502 (2005).

[17] R. Prevedel, P. Walther, F. Tiefenbacher, P. Böhi, R. Kaltenbaek, T. Jennewein, and A. Zeilinger, Nature (London) **445**, 65 (2007).

[18] G. Vallone, E. Pomarico, P. Mataloni, F. De Martini, and V. Berardi, Phys. Rev. Lett. **98**, 180502 (2007).

[19] W.-B. Gao, C.-Y. Lu, X.-C. Yao, P. Xu, O. Gühne, A. Goebel, Y.-A. Chen, C.-Z. Peng, Z.-B. Chen, and J.-W. Pan, Nat. Phys., doi:10.1038/nphys1635.
[20] Y. Tokunaga, S. Kuwashiro, T. Yamamoto, M. Koashi, and N. Imoto, Phys. Rev. Lett. **100**, 210501 (2008).
[21] A. Mair, A. Vaziri, G. Weihs, and A. Zeilinger, Nature (London) **412**, 313 (2001).
[22] C. Cinelli, M. Barbieri, R. Perris, P. Mataloni, and F. De Martini, Phys. Rev. Lett. **95**, 240405 (2005).
[23] M. Barbieri, C. Cinelli, P. Mataloni, and F. De Martini, Phys. Rev. A **72**, 052110 (2005).
[24] J. T. Barreiro, N. K. Langford, N. A. Peters, and P. G. Kwiat, Phys. Rev. Lett. **95**, 260501 (2005).
[25] C. Schuck, G. Huber, C. Kurtsiefer, and H. Weinfurter, Phys. Rev. Lett. **96**, 190501 (2006).
[26] H. S. Park, J. Cho, J. Y. Lee, D.-H. Lee, and S.-K. Choi, Opt. Express **15**, 17960 (2007).
[27] B. P. Lanyon, M. Barbieri, M. P. Almeida, T. Jennewein, T. C. Ralph, K. J. Resch, G. J. Pryde, J. L. O'Brien, A. Gilchrist, and A. G. White, Nat. Phys. **5**, 134 (2009).
[28] G. Vallone, R. Ceccarelli, F. De Martini, and P. Mataloni, Phys. Rev. A **79**, 030301(R) (2009).
[29] R. Ceccarelli, G. Vallone, F. De Martini, P. Mataloni, and A. Cabello, Phys. Rev. Lett. **103**, 160401 (2009).
[30] D. F. V. James, P. G. Kwiat, W. J. Munro, and A. G. White, Phys. Rev. A **64**, 052312 (2001).
[31] M. A. Nielsen, Phys. Rev. Lett. **93**, 040503 (2004).
[32] R. Raussendorf, D. E. Browne, and H. J. Briegel, Phys. Rev. A **68**, 022312 (2003).
[33] W.-B. Gao, P. Xu, X.-C. Yao, O. Gühne, A. Cabello, C.-Y. Lu, C.-Z. Peng, Z.-B. Chen, and J.-W. Pan, Phys. Rev. Lett. **104**, 020501 (2010).
[34] P. G. Kwiat, K. Mattle, H. Weinfurter, A. Zeilinger, A. V. Sergienko, and Y. Shih, Phys. Rev. Lett. **75**, 4337 (1995).
[35] A. Rossi, G. Vallone, A. Chiuri, F. De Martini, and P. Mataloni, Phys. Rev. Lett. **102**, 153902 (2009).
[36] J. D. Franson, Phys. Rev. Lett. **62**, 2205 (1989).
[37] J. Brendel, N. Gisin, W. Tittel, and H. Zbinden, Phys. Rev. Lett. **82**, 2594 (1999).
[38] E. Nagali, L. Sansoni, F. Sciarrino, F. De Martini, L. Marrucci, B. Piccirillo, E. Karimi, and E. Santamato, Nat. Photonics **3**, 720 (2009).
[39] A. Politi, M. J. Cryan, J. G. Rarity, S. Yu, and J. L. O'Brien, Science **320**, 646 (2008).
[40] A. Politi, J. C. F. Matthews, and J. L. O'Brien, Science **325**, 1221 (2009).
[41] J. Matthews, A. Politi, A. Stefanov, and J. L. O'Brien, Nat. Photonic **3**, 346 (2009).
[42] G. D. Marshall, A. Politi, J. C. F. Matthews, P. Dekker, M. Ams, M. J. Withford, and J. L. O'Brien, Opt. Express **17**, 12546 (2009).